Journal Pre-proofs

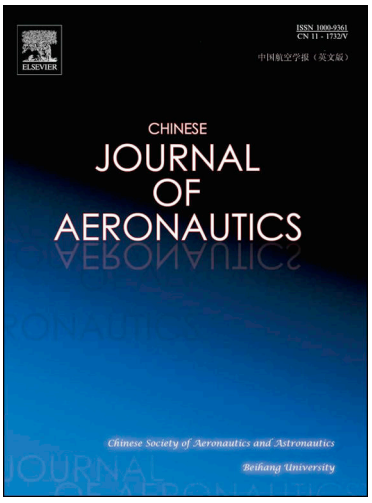


# Taylor-Couette instability with differential slip at one boundary

Giulia INNOCENTI, Edoardo MAESTRI, Giovanni BESTOSO, Alberto LAGAZZO, Marina DELUCCHI, Enzo SANTOROMITO, Nicolas MAZELLIER, Jan O. PRALITS, Alessandro BOTTARO

PII: S1000-9361(26)00143-3
DOI: https://doi.org/10.1016/j.cja.2026.104206
Reference: CJA 104206

To appear in: *Chinese Journal of Aeronautics*

Received Date: 24 November 2025
Revised Date: 8 April 2026
Accepted Date: 8 April 2026

Please cite this article as: G. INNOCENTI, E. MAESTRI, G. BESTOSO, A. LAGAZZO, M. DELUCCHI, E. SANTOROMITO, N. MAZELLIER, J.O. PRALITS, A. BOTTARO, Taylor-Couette instability with differential slip at one boundary, *Chinese Journal of Aeronautics* (2026), doi: https://doi.org/10.1016/j.cja.2026.104206

# Taylor-Couette instability with differential slip at one boundary

Giulia INNOCENTI[a], Edoardo MAESTRI[b], Giovanni BESTOSO[b], Alberto LAGAZZO[a], Marina DELUCCHI[a], Enzo SANTOROMITO[c], Nicolas MAZELLIER[c], Jan O. PRALITS[a], Alessandro BOTTARO[a,*]

[a]*Department of Civil, Chemical and Environmental Engineering, Scuola Politecnica, Università di Genova, via Montallegro 1, Genova 16145, Italy*
[b]*Department of Mechanical, Energy, Management and Transport Engineering, Scuola Politecnica, Università di Genova, via Montallegro 1, Genova 16145, Italy*
[c]*PRISME laboratory, University of Orléans , 8 Rue Léonard de Vinci, Orléans 45072, France*

Received 24 November 2025; revised 24 December 2025; accepted 20 January 2026

**Abstract**

A comprehensive study is conducted to assess the effect that circumferential microgrooves positioned on the inner wall of a Taylor-Couette system have on the onset of the primary linear instability. Experiments are conducted on an apparatus in which the wall corrugations are produced by stereolithographic printing and critical parameters are estimated primarily by measuring the torque on the inner cylinder as function of the angular velocity of rotation. An asymptotic upscaling analysis is then conducted to estimate the slip lengths (azimuthal and axial) of the axially-periodic microgrooves, i.e. the radial distances from the reference radius $R_i$ where the azimuthal and radial velocity components extrapolate to zero. Using such lengths, a linear stability analysis is carried out to infer the critical parameters for the onset of Taylor rolls under conditions of differential slip. The experimental-theoretical results are in good agreement with one another, and appear to show that the instability is promoted by the grooves. However, when *virtual* dimensions are introduced to account for the virtual origin of the mean azimuthal flow, and the parameters are properly rescaled, it is demonstrated that the instability is, in fact, delayed by the wall corrugations, and more so for larger differential slip, i.e. when the azimuthal slip length exceeds its spanwise counterpart by a larger margin.

*Keywords:* Taylor-Couette instability; Riblets; Slip flow; Upscaling theory; Linear stability analysis

*Corresponding author. E-mail address: alessandro.bottaro@unige.it (A. BOTTARO)

## 1. Introduction

The Taylor-Couette (TC) instability between two concentric, differentially rotating cylinders is a prototypical example of hydrodynamic system for which excellent agreement is found between theoretical and experimental results. The ground-breaking, 1923 paper by Taylor,[1] beyond resolving conclusively the problem of the stability of the Couette flow in a curved geometry, provided compelling evidence for the applicability of the no-slip boundary condition (a topic of debate in the 19th century) in practical fluid flow systems.

The focus of the present paper is on the potentially unstable case of the outer cylinder at rest, while the inner cylinder is forced to rotate at angular velocity $\Omega = \frac{\pi}{30}\dot{n}$ (with $\Omega$ denoting the angular velocity measured in radians per second and $\dot{n}$ the rpm velocity). If the walls of the cylinders are smooth, and their inner and outer radii are, respectively, $R_i$ and $R_o$, the control parameter is the Taylor number, $Ta$, conventionally defined as

$$Ta = \frac{2\,\eta^2}{1-\eta^2} \cdot \frac{\Omega^2\, d^4}{\nu^2} = Re^2\, \frac{2\,d}{R_i + R_o} \tag{1}$$

In the expression above, $d = R_o - R_i$ is the gap between the cylinders, $\eta = R_i/R_o$ is the radius ratio and $\nu$ is the kinematic viscosity of the fluid. The parameter $Re$ is the Reynolds number, defined as $Re = \Omega R_i\, d/\nu$. In the so-called narrow gap case, when $\eta \to 1$, the onset of steady toroidal vortices is found for the following *critical* parameters: $Ta_c = 1708$ and $\beta_c = 3.117$,[2] with $\beta$ the axial wavenumber.

In the recent past, much attention has been paid to the case of non-smooth walls, for example rough surfaces which are superhydrotolitobic or impregnated with a liquid lubricant, or just micro-textured. Interest in these cases has arisen because of the potential for drag reduction provided by such *slip* surfaces, in laminar and turbulent conditions.

For the flow between co-rotating cylinders, skin friction drag is affected most notably under turbulent flow conditions. The experimental work by Srinivasan et al.[3] demonstrated a reduction in the measured inner wall shear stress in moderately turbulent TC flows when sprayable superhydrophobic particles were deposited on the inner rotor surface. The magnitude of reduction becomes progressively larger as the Reynolds number increases, up to a value of 22% at the maximum Reynolds number, $Re = 8 \times 10^4$, attainable by the apparatus. The findings of this paper suggest that superhydrophobic coatings can provide a sustainable method for drag reduction in turbulent flows. A subsequent work by Naim and Baig[4] investigated by direct numerical simulations the impact of various superhydrophobic surface patterns on drag reduction in turbulent TC flows. The authors explored different configurations, modeling the plastron-liquid interface as undeformable, shear-free areas, to find that streamwise-aligned microgrooves led to the highest drag reduction, achieving up to 34% at $Re = 5000$. In contrast, spiral grooves resulted in a mild drag enhancement. The simulations showed that superhydrophobic wall configurations produced surface slip which modified the near-wall turbulence dynamics. These modifications influence the production of near-wall streamwise velocity fluctuations and turbulence kinetic energy, contributing to the observed drag reduction. A recent study by Liu et al.[5] employed a combination of experimental measurements and theoretical modeling to understand the mechanisms behind drag reduction

when air-filled V-shaped azimuthal microgrooves covered the inner, rotating cylinder of a TC system. The study reported a drag reduction of up to 62% when the Reynolds number attained the value of $2.79 \times 10^4$. Stable and robust superhydrophobicity was maintained by applying on the grooves a styrene-ethylene-butylene-styrene copolymer coating and by treating the tips of the V-grooves to be hydrophilic. The air-filled azimuthally-invariant corrugations induced wall slip, which weakened the intensity of Taylor rolls and reduced local momentum transport, leading to lower drag. Increasing the groove width enhanced wall slip favoring drag reduction, with the relationship between drag reduction and groove spacing well-predicted by a model based on angular momentum defect theory.

The case of corrugated surfaces impregnated with a liquid lubricant was considered by Van Buren and Smits;[6] they described measurements in an apparatus with lubricant-impregnated microgrooves in the inner cylinder of a TC apparatus. The study reported a maximum drag reduction of approximately 45% at a Reynolds number of around $10^4$; the reduction was found to be stable over time, indicating the potential for sustainable performance of lubricant-impregnated surfaces in practical applications.

In the absence of a lubricant fluid, longitudinal microgrooves take the name of riblets.[7–9] In the context of turbulent TC flow, the study of V-shaped azimuthal riblets was initiated by Hall and Joseph;[10] their focus was on the effectiveness of riblets to reduce skin friction drag, in a setup where the inner cylinder was corrugated and only the outer cylinder was forced to rotate. A more detailed analysis, including tomographic PIV measurements, was later carried out by Greidanus et al.;[11] their work included a simple model to distinguish between the contributions of riblets and rotation (of either cylinder) to drag reduction. It was found that the friction coefficient of riblets was strongly determined by the flow regimes and that, above a threshold shear-velocity-Reynolds number, a drag reduction of up to 3.4% was possible. The recent PIV experiments by Xu et al.[12] are the only ones we are aware of which do not focus exclusively on the turbulent regime. They considered a variety of V-shaped azimuthal riblets, machined on the inner, rotating cylinder of a TC setup, and conducted tests for $Re$ as low as 160 (very close to the onset of wavy vortex flow), up to 18700. The transition to the turbulent regime was quantified to occur for $Re_{\mathrm{trans}} \approx 1380$ in a setup with $\eta = 0.7$. At $Re < Re_{\mathrm{trans}}$ they found that the weakening of the primary Taylor vortices was responsible for drag reduction (with further reduction in the measured torque as $Re$ and the size of the microgrooves was increased). Above the threshold $Re_{\mathrm{trans}}$, roughness was responsible for an increase in drag. The immersed-boundary, direct numerical simulations of Zhu et al.[13] reinforced the conclusions by Xu et al.[12] relative to the high-$Re$ regimes, showing how V-shaped grooves on the walls altered the torque scaling behavior and flow structures. In the weak turbulence regime the effect of grooves appeared to be mild; with the increase in $Re$, the boundary layer became thinner than the groove height and the wall corrugations induced secondary flows, enhancing the torque. This led to a steeper scaling exponent, which eventually saturated back to the ultimate regime value at higher Reynolds numbers.

Whereas the influence of riblets on the modal and nonmodal instability of the laminar flow in a plane channel has already been addressed,[14] to the best of the present authors' knowledge no studies are available on the effect of rough surfaces on the primary TC insta-

bility. This problem is of interest in itself, to inform on whether specific roughness textures can delay or anticipate transition initiated by streamwise vortices, and also because it represents the necessary first step before proceeding to more complex configurations, with higher rotation speed, using superhydrophobic or lubricant-infused surfaces, etc. An additional aspect to bear in mind is the fact that the centrifugal force can produce and sustain, even at relatively low velocities, vortical structure which function as organizing frameworks for the transport of energy and momentum, analogous to the role played by near-wall streaks and quasi-streamwise vortices in structuring turbulence production in wall-bounded shear flows.

The present work addresses these open issues by providing the first combined experimental and theoretical investigation of the primary TC instability in the presence of axially periodic, azimuthally invariant wall corrugations. The novelty of the study lies in: (A) the use of torque-based measurements to quantify the onset of the primary instability for micro-grooved inner cylinders; (B) the derivation of anisotropic effective slip lengths for realistic, three-dimensional printed grooves via asymptotic homogenization; (C) the incorporation of these effective boundary conditions into a linear stability analysis; and (D) the demonstration that the apparent destabilization observed in physical coordinates is reconciled by introducing a virtual origin of the mean azimuthal flow, revealing instead a systematic delay of the instability governed by the differential slip length. Together, these elements provide a unified framework to interpret and predict the influence of wall micro-structuring on centrifugal instabilities.

## 2. Experimental apparatus and results

### *2.1. Description of experimental apparatus*

The experimental apparatus is shown in Fig. 1. It is based on the Anton Paar Physica MCR 301 rheometer, with an inner shaft which rotates via a highly precise rotational electric motor supported by an air bearing. This ensures virtually frictionless rotation and high sensitivity for torque and angular displacement, enabling accurate measurements for all conditions tested. The torque is measured by a strain-gauge-based transducer with resolution in the nanoNewton meter range, while the angular velocity is controlled and measured by an electrically commutated synchronous motor with optical encoders which provide extremely precise angular position data from which velocity is derived. The shaft is connected to the internal rotating cylinder which is freely suspended and terminates with a conical tip (dimensions are given in Fig. 1), inserted coaxially into a fixed cylindrical plexiglass case. The inner element turns around its axis at angular speed $\Omega$, causing the motion of the water within the test section and, eventually, the formation of secondary, Taylor-Couette, vortices. The water has a free surface exactly in correspondence with the outer edge of the inner cylinder, which remains wet throughout each test; we have verified that the free surface remains flat and unperturbed when the angular velocity of rotation is sufficiently small, while low-amplitude surface waves develop at larger velocities. Since our interest here is on the primary instability, we consider acceptable this arrangement. The presence of a bottom region, below the test cylinder, where the water is set into motion by the rotation of the lower cone, is accounted for as discussed in Appendix A.

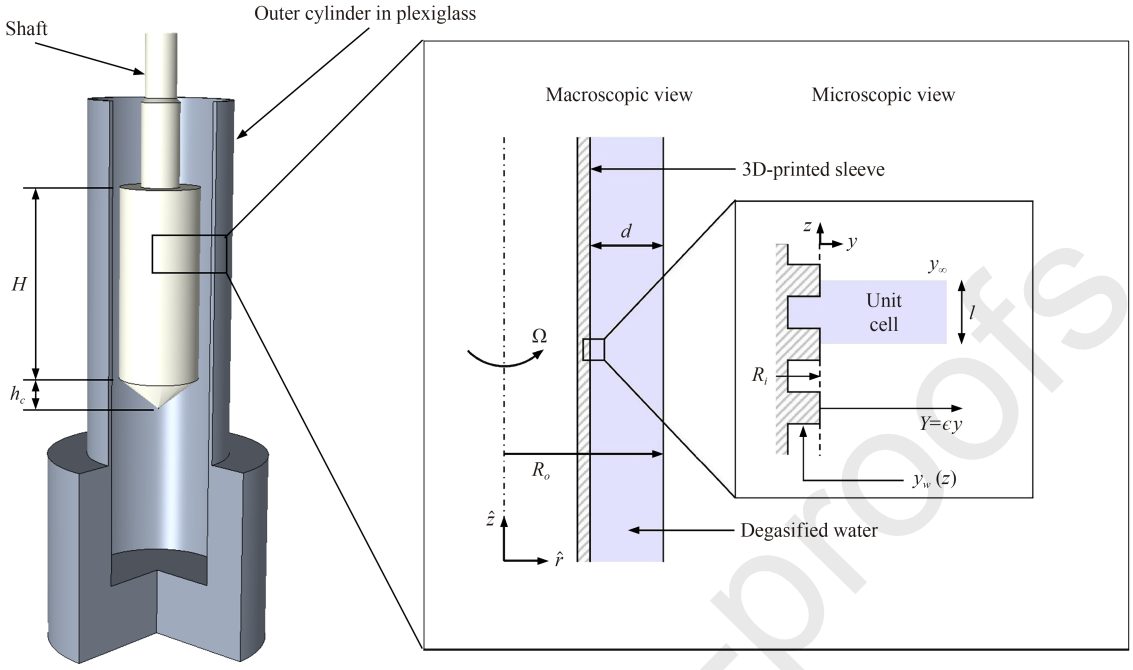


Fig. 1 Schematic of apparatus, shown to scale, without micro-corrugated sleeve around cylinder (left image).

The inner cylinder has a diameter of 25 mm; the height of the inner cylinder is $H = 60$ mm and that of the bottom cone is $h_c = 10$ mm. In the inset on the right, macroscopic and microscopic sketches of the system, including the 3D-printed micro-grooves, are drawn, not to scale, with dimensional and dimensionless axes. On the extreme right frame, the unit cell of the homogenization problem is also shown. The axial periodicity of the roughness, $\ell$, is the microscopic length scale while the gap dimension, $d = R_o - R_i$, is the macroscopic scale; their ratio define the small parameter $\epsilon$ of the asymptotic expansion of Section 3. The equation of the rough wall is $y = y_w(z) \leq 0$.

Polymeric *sleeves* with different micro-structured patterns are 3D-printed and placed around the inner cylinder, to study the effect of azimuthally-invariant surface structures on the onset of the instability; they are shown on the right sketch of Fig. 1. Whereas the inner radius $R_i$ of the cylinder plus sleeve is approximately 19 mm (the exact dimensions, given further down, depend on the micro-pattern and on the pitch $\ell$ of the corrugations), the outer radius $R_o$ is fixed and equal to 20.64 mm.

### *2.2. Microstructured* sleeves *around inner cylinder*

The different micro-structured sleeves are obtained by a laser-powered stereolithographic printer produced by Formlabs (model Form3), an additive manufacturing technology for thermosetting polymers. The method is based on the photopolymerization of a liquid resin sensitive to the ultraviolet radiation emitted by a laser source; the technique allows, in principle, greater geometric accuracy than normal extrusion 3D printing. The polymeric resin used (Clear Resin, also produced by Formlabs) is specifically designed for high-resolution models.

Before the experiments, the water is properly degasified, to prevent the formation of gas bubbles. Hollow glass beads of diameter equal to 10 μm and density very mildly above the density of water (Dantec Dynamics HGS-10 Hollow Glass Spheres) are used to visualize the vortices, and their mass concentration in the water is always kept below 1%. In order to better enhance the contrast with the fluid markers the microstructured sleeves are printed adding a black dye to the transparent resin. Beyond allowing for a better visualization of the flow structures, this procedure also permits the laser analysis of each 3D-printed sample, to assess the exact shape and dimensions of the micro-patterns.

Two types of azimuthally-invariant shapes are designed for later printing; a trapezoidal shape and a square one (denoted respectively by "$T$" and "$S$"). They are shown in Fig. 2; later on, these shapes will also be referred to as *idealized* shapes. The axial periodicity $\ell$ of the periodic pattern is set to be either 1000 μm, 800 μm or 400 μm. The different patterns are thus named $T1000$, $S800$ etc., to distinguish among them.

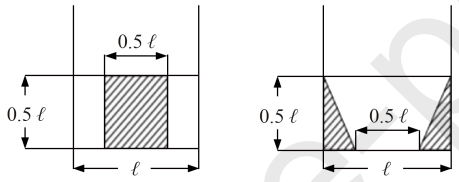


Fig. 2 Idealized shape of unit cells for $S$ and $T$ micro-grooves.

Upon stereolithographic printing, the patterns of the different micro-grooves display differences from the idealized ones, because of limitations related to "stair-stepping" artifacts on sloped surfaces and to shrinkage/distortion of the photopolymer resins during curing. Samples of surface area equal to 3 mm × 3 mm are scanned with the Taylor Hubson laser profilometer (Ametek's Ultra Precision Technologies Group) and typical results, reconstructed on a planar surface, are displayed in Fig. 3. These are referred, later on, as the *realistic* patterns. Optical microscopy of all samples is also performed, and two typical images are provided in Fig. 4; the right image highlights the presence of a defect in the microstructure, probably arising from the mechanical setup of the 3D printer.

The dimensions of the printed samples are reported in Table 1. The measurements of $\ell$ arise directly from the laser scans and from optical microscopy, while the dimensions $R_i$, $R_o$ and $H$ are obtained with a digital caliper with a resolution of 0.01 mm. All measurements have been taken at a dozen different positions (both along the axial and the azimuthal direction, depending on what is being measured) to obtain average values and assess the variability of the signals. The root mean square (rms) deviation on the measurements of $H$ is always lower than 0.20 mm for all samples tested, while the rms error on $R_i$ and $R_o$ remains below 0.08 mm. As far as the periodicity $\ell$ of the ribs, the deviation from the nominal value is always below 0.01 mm (Fig. 4, left frame).

### *2.3. Results of experiments*

The first case examined is that of the cylinder with a smooth sleeve, for which $\eta = 0.890$. The results for this case can be extrapolated from old data in the literature (see, e.g., Table

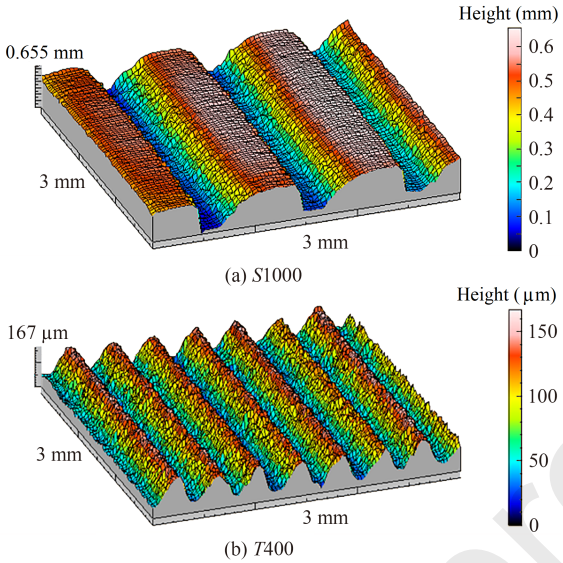


Fig. 3 Three-dimensional, reconstructed shapes of effective, 3D-printed azimuthally-invariant micro-ribs at inner cylinder wall.

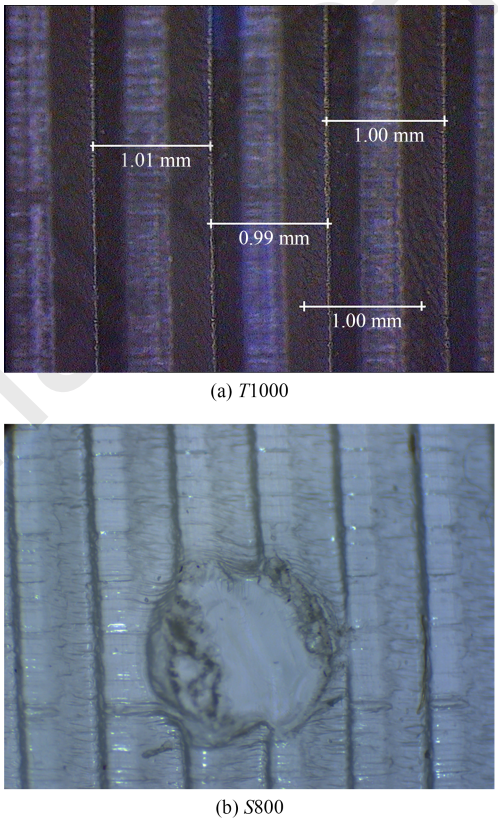


Fig. 4 Optical microscopy of two ribbed surfaces, $T1000$ (measured periodicity $\ell$ is indicated) and $S800$ (with a defect).

Table 1 Measurements of stereolithography-printed micro-roughness elements.

| Case | $R_i$ (mm) | $R_m$ (mm) | $d$ (mm) | $\ell$ (mm) | $\eta = R_i/R_o$ | $\delta = d/R_i$ | $\epsilon = \ell/d$ |
|---|---|---|---|---|---|---|---|
| Smooth cylinder | 18.36 | 19.50 | 2.28 | | 0.890 | 0.124 | |
| $T400$ | 18.70 | 19.67 | 1.94 | 0.40 | 0.906 | 0.104 | 0.206 |
| $T800$ | 18.85 | 19.74 | 1.79 | 0.80 | 0.913 | 0.095 | 0.447 |
| $T1000$ | 18.95 | 19.79 | 1.69 | 1.00 | 0.918 | 0.089 | 0.592 |
| $S800$ | 18.82 | 19.73 | 1.82 | 0.80 | 0.912 | 0.097 | 0.440 |
| $S1000$ | 18.96 | 19.80 | 1.68 | 1.00 | 0.919 | 0.089 | 0.595 |

Notes: for the case labelled "smooth cylinder", a smooth polymeric sleeve of thickness equal to 5.86 mm is positioned around the inner, stainless steel cylinder. Each sleeve is $H = 60$ mm high, within $\pm 0.20$ mm, i.e. the inner cylinder is completely covered. $R_m = (R_i + R_o)/2$ is the mean radius; $\delta$ is the curvature parameter and $\epsilon$, used in the homogenization analysis, is the ratio of microscale to macroscale.

11.1 in Koschmieder[15] based on calculations conducted by P.H. Roberts in 1965) giving $Ta_c = 1839$ and $\beta_c = 3.129$. Our own results (see later in Section 4 for details of the stability analysis and computations) for the case of no-slip boundaries are $Ta_c = 1735$ and $\beta_c = 3.143$, i.e. the critical Taylor number is some 5.7% smaller than the reference value, while the wavenumber is less than 0.5% away from the number reported by Koschmieder. This disagreement with respect to published data might, in part, stem from uncertainties in our small perturbation theory, where terms of order two (i.e., $\epsilon^2$, $\epsilon\delta$, and $\delta^2$) are neglected. It is also quite possible that the old results from the literature are not entirely accurate.

The experiments are conducted by rapidly taking the shaft to an angular velocity equal to $\dot{n} = 20$ r/min, followed by a waiting period of several minutes until the steady state is achieved; then, the speed of rotation is raised in steps of 0.5 r/min, and kept at the new value for a duration of 30 s up to 50 r/min, with the torque recorded. This duration has been chosen upon considering that the diffusion time scale, $d^2/\nu$, is of the order of five seconds. Its appropriateness has been verified by carrying out several tests with the angular velocity maintained constant for up to 10 minutes, recovering in each test the same value of the torque as in the more rapidly evolving protocol. The chosen combination of rpm-step size and relaxation time ensures that the process is quasi-static, with the water temperature and the viscosity varying only mildly during each experiment. Transition is classically observed when the slope of the torque curve changes suddenly with $\dot{n}$, a sign that rolls have appeared, modifying the shear stress at the wall. The onset of the secondary and successive instabilities can likewise be detected. Each experiment is repeated multiple times to confirm results, including both positive and negative increments in angular velocity to rule out possible hysteresis effects, and lasts half an hour; during each test the increase in water temperature because of viscous heating is less than 0.5 °C. The water temperature is measured and monitored with thermocouples; from one trial to the next its value can go from a minimum of 24 °C to a maximum of 26 °C, remaining in all cases constant along the height of the cylinder. The normalization of the measured torque and angular velocity (to yield the torque coefficient, defined later, and the Reynolds number) always refer to

the mean density and kinematic viscosity of the specific experiment. In the temperature range from 24 °C - 26 °C, the density $\rho$ changes mildly from 997.3 to 996.8 kg/m$^3$ while the kinematic viscosity $\nu$ decreases from $0.9132 \times 10^{-6}$ to $0.8729 \times 10^{-6}$ m$^2$/s.

An example of dimensional results is presented in Appendix A, together with a discussion on cylinder end effects. All the other results presented herein are in dimensionless form, after the torque $\mathcal{C}$ and the angular velocity are properly scaled to yield a torque coefficient and a Taylor number. The former is defined as

$$c_T = \frac{\mathcal{C}}{\pi \rho \Omega^2 R_i^4 H} \tag{2}$$

Results in dimensionless form are displayed in Fig. 5 for both trapezoidal and square grooves. For all wall patterns the primary instability appears in the form of a sudden slope change around $Ta$ equal 1700 (precise values are provided later); a secondary instability to wavy vortex flow is also visible from the figure somewhat after a Taylor number of 2000. The trend of the primary breakdown for the case of $T$ corrugations does not appear to be monotonic with the pitch of the grooves: the first bifurcation for $\ell = 800\,\mu$m (red curves) occurs before the other two cases (precise values are given later in Table 5). This is only an apparent contradiction; first, dimensionless values of $Re$ and $Ta$ can be compared between two different configurations only at a fixed radius ratio (and here the values of $\eta$ vary, albeit mildly, from one configuration to the next, Table 1). Furthermore, the different cases examined present different *virtual origins* of the primary motion. A discussion on this aspect, and its consequences, is deferred until Section 4.

Sample visualizations are shown in Fig. 6 for the case $T800$, both slightly before and slightly after the first instability. In the left frame only the grooves are visible, while in the right frame the presence of glass beads in the water allows to visualize the formation of rolls; the white, regularly spaced stripes in the right image highlight the presence of sinks, location of radial inward motion. Since the glass beads can easily be trapped within the cavities formed between adjacent grooves, it is difficult to measure with the necessary precision the axial wavelength of the vortices. It is also possible that the presence of the grooves contributes in receptively determining the wavenumber of the instability since, as shown later, curves of constant amplification in the vicinity of the onset of the instability are quite "flat" around $\beta = 3$, highlighting the weak wavenumber selectivity of the Taylor vortices. Wavenumber values, provided later, are obtained by averaging over the six central pairs of rolls; a Fujifilm XT200 (18-35 mm) mirrorless camera is used and the 24 megapixels images are treated using ImageJ software and a caliper as a reference. The experimentally determined wavenumbers are given with only two significant digits because of difficulties in precisely defining the boundaries of each pair of rolls.

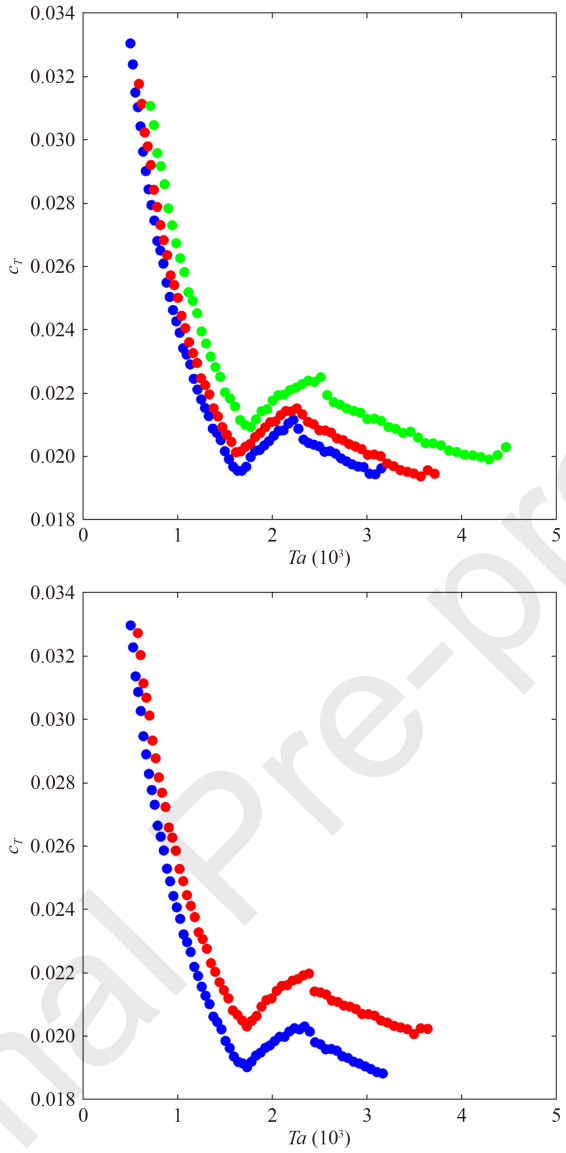


Fig. 5 Data of torque coefficient versus Taylor number for trapezoidal (up) and square (down) surface corrugations (Green markers corresponds to $\ell = 400$ µm; red and blue markers represent data of cases $\ell = 800$ µm and $\ell = 1000$ µm, respectively).

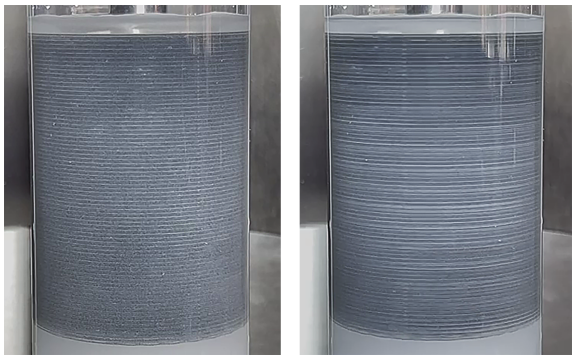

Fig. 6 Visualizations of motion before (left) and after (right) onset of first bifurcation for case $T800$.

## 3. Asymptotic homogenization theory for *effective* boundary conditions

The presence of axially periodic, azimuthally invariant microgrooves at the wall of the inner cylinder suggests the use of homogenization theory to infer effective boundary conditions at a fictitious boundary, taken here to coincide with $y = 0$ (see the microscopic view in Fig. 1). Such effective conditions, available when the length scale of the surface corrugations is much smaller than the characteristic macroscopic scale (here taken to coincide with the gap width, $d$), allow us to avoid the (computationally more expensive) numerical solution of a macroscopic problem with no-slip boundaries at the real corrugated wall in $y = y_w(z)$. The theory builds upon recent contributions[16–21] to yield azimuthal and axial *Navier slip lengths* for different shapes and dimensions of the surface corrugations.

The analysis starts from the mass-conservation and Navier-Stokes equations in cylindrical coordinates, for the case of axisymmetric flows:

$$\frac{\partial \hat{u}_r}{\partial \hat{r}} + \frac{\hat{u}_r}{\hat{r}} + \frac{\partial \hat{u}_z}{\partial \hat{z}} = 0 \tag{3}$$

$$\rho\left(\frac{\partial \hat{u}_r}{\partial \hat{t}} + \hat{u}_r\frac{\partial \hat{u}_r}{\partial \hat{r}} + \hat{u}_z\frac{\partial \hat{u}_r}{\partial \hat{z}} - \frac{\hat{u}_\theta^2}{\hat{r}}\right) = -\frac{\partial \hat{p}}{\partial \hat{r}} + \mu\left(\frac{\partial^2 \hat{u}_r}{\partial \hat{r}^2} + \frac{1}{\hat{r}}\frac{\partial \hat{u}_r}{\partial \hat{r}} - \frac{\hat{u}_r}{\hat{r}^2} + \frac{\partial^2 \hat{u}_r}{\partial \hat{z}^2}\right) \tag{4}$$

$$\rho\left(\frac{\partial \hat{u}_\theta}{\partial \hat{t}} + \hat{u}_r\frac{\partial \hat{u}_\theta}{\partial \hat{r}} + \hat{u}_z\frac{\partial \hat{u}_\theta}{\partial \hat{z}} + \frac{\hat{u}_\theta\,\hat{u}_r}{\hat{r}}\right) = \mu\left(\frac{\partial^2 \hat{u}_\theta}{\partial \hat{r}^2} + \frac{1}{\hat{r}}\frac{\partial \hat{u}_\theta}{\partial \hat{r}} - \frac{\hat{u}_\theta}{\hat{r}^2} + \frac{\partial^2 \hat{u}_\theta}{\partial \hat{z}^2}\right) \tag{5}$$

$$\rho\left(\frac{\partial \hat{u}_z}{\partial \hat{t}} + \hat{u}_r\frac{\partial \hat{u}_z}{\partial \hat{r}} + \hat{u}_z\frac{\partial \hat{u}_z}{\partial \hat{z}}\right) = -\frac{\partial \hat{p}}{\partial \hat{z}} + \mu\left(\frac{\partial^2 \hat{u}_z}{\partial \hat{r}^2} + \frac{1}{\hat{r}}\frac{\partial \hat{u}_z}{\partial \hat{r}} + \frac{\partial^2 \hat{u}_z}{\partial \hat{z}^2}\right) \tag{6}$$

with $\hat{u}_r, \hat{u}_\theta$ and $\hat{u}_z$ the three velocity components along the directions denoted by the respective subscripts, $\hat{p}$ the pressure, $\rho$ the density and $\mu$ the dynamic viscosity of the fluid contained within the two co-axial cylinders.

The theory relies on dividing the whole flow domain into two parts, an inner microscopic part, ruled by viscous diffusion, and an outer macroscopic portion where inertia is important; the two domains are scaled differently and are matched through the continuity of velocity and traction vectors at their interface. The latter is situated at a distance from the real wall which is very small when measured in outer coordinates, but very large when observed in inner

coordinates. The inner and outer domains are sketched in Fig. 1. In the microscopic region, located near the microstructured wall, the characteristic dimension is $\ell$; in the macroscopic outer region the characteristic dimension is $d$. The homogenized model is formally derived under the assumption $\epsilon \equiv \ell/d \ll 1$. On the other hand, we note that it is common in practice for leading-order descriptions to remain accurate for moderately small values of $\epsilon$. The results described in the following, where $\epsilon$ is not infinitesimal, should therefore be interpreted as indicative rather than asymptotically exact.

The dimensionless, macroscopic variables in the outer region are defined using capital letters (aside for time which is denoted by $\tau$) as follows:

$$\begin{cases} \tau = \dfrac{\hat{t}}{d/(\Omega R_i)} \\ Y = \dfrac{\hat{r} - R_i}{d} \\ Z = \dfrac{\hat{z}}{d} \\ (U, V, W) = \dfrac{(\hat{u}_\theta, \hat{u}_r, \hat{u}_z)}{\Omega R_i} \\ P = \dfrac{\hat{p}}{\rho(\Omega R_i)^2} \end{cases} \tag{7}$$

for the equations to read

$$\frac{\partial V}{\partial Y} + \delta V + \frac{\partial W}{\partial Z} = 0 \tag{8}$$

$$\frac{\partial V}{\partial \tau} + V\,\frac{\partial V}{\partial Y} - \delta\, U^2 + W\,\frac{\partial V}{\partial Z} = -\frac{\partial P}{\partial Y} + \frac{1}{Re}\left(\frac{\partial^2 V}{\partial Y^2} + \delta\frac{\partial V}{\partial Y} + \frac{\partial^2 V}{\partial Z^2}\right) \tag{9}$$

$$\frac{\partial U}{\partial \tau} + V\,\frac{\partial U}{\partial Y} + \delta\, U V + W\,\frac{\partial U}{\partial Z} = \frac{1}{Re}\left(\frac{\partial^2 U}{\partial Y^2} + \delta\frac{\partial U}{\partial Y} + \frac{\partial^2 U}{\partial Z^2}\right) \tag{10}$$

$$\frac{\partial W}{\partial \tau} + V\,\frac{\partial W}{\partial Y} + W\,\frac{\partial W}{\partial Z} = -\frac{\partial P}{\partial Z} + \frac{1}{Re}\left(\frac{\partial^2 W}{\partial Y^2} + \delta\frac{\partial W}{\partial Y} + \frac{\partial^2 W}{\partial Z^2}\right) \tag{11}$$

with $Re = \dfrac{\rho\,\Omega\,R_i\,d}{\mu}$ the Reynolds number and $\delta = d/R_i$ the curvature parameter. The system above is correct up to order $\delta$, under the assumption that $\delta \ll 1$. It is important to note that, provided $Y_\infty \leq Y \leq 1$, the variables $(U, V, W, P)$ depend only on the macroscopic dependent variables $Y$ and $Z$. The boundary at $Y = 1$ satisfies the simple no-slip condition.

The microscales in the near-wall domain are

$$\begin{cases} y = \dfrac{\hat{r} - R_i}{\epsilon\, d} \\ z = \dfrac{\hat{z}}{\epsilon\, d} \\ (u, v, w) = \dfrac{(\hat{u}'_\theta, \hat{u}_r, \hat{u}_z)}{\epsilon\, \Omega\, R_i} \\ P = \dfrac{\hat{p}}{\mu\, \Omega\, R_i / d} \end{cases} \tag{12}$$

with $\hat{u}'_\theta = \hat{u}_\theta - \Omega\, R_i$ the azimuthal velocity deviation, for the steady, creeping flow equations in the inner region, neglecting terms of order $\delta^2$, $\epsilon^2$, $\epsilon\,\delta$ and higher, to read

$$\frac{\partial v}{\partial y} + \frac{\partial w}{\partial z} = 0 \tag{13}$$

$$-\frac{\partial p}{\partial y} + \frac{\partial^2 v}{\partial y^2} + \frac{\partial^2 v}{\partial z^2} = 0 \tag{14}$$

$$\frac{\partial^2 u}{\partial y^2} + \frac{\partial^2 u}{\partial z^2} = 0 \tag{15}$$

$$-\frac{\partial p}{\partial z} + \frac{\partial^2 w}{\partial y^2} + \frac{\partial^2 w}{\partial z^2} = 0 \tag{16}$$

The boundary conditions for the inner problem on the real wall in $y_w(z)$ are simply $u = \delta\, y_w, v = w = 0$. On the outer boundary, where $Y_\infty = \epsilon\, y_\infty$, the microscopic fields become independent of $z$ provided $y_\infty$ is chosen sufficiently far from $y_w$; matching dimensionless velocity and traction vectors leads to

$$\begin{cases} U\big|_{Y_\infty} = 1 + \epsilon\, u\big|_{y_\infty} \\ V\big|_{Y_\infty} = \epsilon v\big|_{y_\infty} \\ W\big|_{Y_\infty} = \epsilon w\big|_{y_\infty} \end{cases} \tag{17}$$

$$\left.\frac{\partial U}{\partial Y}\right|_{Y_\infty} = \left.\frac{\partial u}{\partial y}\right|_{y_\infty} \tag{18}$$

$$-Re\, P + 2\left.\frac{\partial V}{\partial Y}\right|_{Y_\infty} = -p + 2\left.\frac{\partial v}{\partial y}\right|_{y_\infty} \tag{19}$$

$$\left.\frac{\partial V}{\partial Z} + \frac{\partial W}{\partial Y}\right|_{Y_\infty} = \left.\frac{\partial v}{\partial z} + \frac{\partial w}{\partial y}\right|_{y_\infty} \tag{20}$$

Given that the problem for $u$ is decoupled from the others, and on account of the terms forcing the problem, the solution for the dimensionless azimuthal velocity can be readily expressed as

$$u = u^\dagger(y,z)\left.\frac{\partial U}{\partial Y}\right|_{Y_\infty} + \delta\, y_w \tag{21}$$

with the auxiliary variable $u^\dagger$ solution of

$$\frac{\partial^2 u^\dagger}{\partial y^2} + \frac{\partial^2 u^\dagger}{\partial z^2} = 0 \tag{22}$$

subject to $u^\dagger = 0$ at $y = y_w$ and $\dfrac{\partial u^\dagger}{\partial y} = 1$ at $y = y_\infty$.

The outer solution, first equation in Eq. (17), can be Taylor expanded,

$$U\big|_{Y_\infty} = U\big|_{Y=0} + \epsilon\, y_\infty \left.\frac{\partial U}{\partial Y}\right|_{Y=0} + \mathcal{O}(\epsilon^2) = 1 + \epsilon\, u^\dagger(y_\infty, z)\left[\left.\frac{\partial U}{\partial Y}\right|_{Y=0} + \mathcal{O}(\epsilon)\right] + \mathcal{O}(\epsilon\,\delta) \tag{23}$$

for the outer condition to be eventually transferred to the fictitious boundary in $Y = 0$; it reads at leading order

$$U\big|_{Y=0} = \epsilon\, \ell_x \left.\frac{\partial U}{\partial Y}\right|_{Y=0} \tag{24}$$

with the slip length $\ell_x = u^\dagger(y_\infty, z) - y_\infty$. Notice that, at $y = y_\infty$, $u^\dagger$ is independent of $z$ and that $\ell_x$ does not vary with the choice of $y_\infty$.

The solution of the other two components of the inner velocity vector, coupled through the pressure, proceeds as in the case of closely-spaced planar riblets;[8,22] provided $y_\infty$ is taken sufficiently far from $y_w$ for the solutions there to become independent of $z$ (as will be shown later) the leading order expressions for the outer velocities become

$$\begin{cases} V\big|_{Y=0} = 0 \\ W\big|_{Y=0} = \epsilon\, \ell_z \left.\dfrac{\partial W}{\partial Y}\right|_{Y=0} \end{cases} \tag{25}$$

with the spanwise slip length defined as $\ell_z = w^\dagger(y_\infty, z) - y_\infty$, independent of the choice of $y_\infty$; the field $(v^\dagger, w^\dagger, p^\dagger)$ solves a Stokes system in the inner domain, subject to no-slip at $y = y_w$ plus $\dfrac{\partial w^\dagger}{\partial y} = 1$ and $v^\dagger = 0$ at $y = y_\infty$.

In dimensional variables the conditions at the boundary at $\hat{r} = R_i$ finally read

$$\begin{cases} \hat{u}_\theta\big|_{r=R_i} = \Omega(R_i + \hat{y}_w) + \hat{\ell}_x \left.\dfrac{\partial \hat{u}_\theta}{\partial \hat{r}}\right|_{r=R_i} \\ \hat{u}_r\big|_{r=R_i} = 0 \\ \hat{u}_z\big|_{r=R_i} = \hat{\ell}_z \left.\dfrac{\partial \hat{u}_z}{\partial \hat{r}}\right|_{r=R_i} \end{cases} \tag{26}$$

The azimuthal slip length $\ell_x = \hat{\ell}_x/\ell$ deserves particular attention for the different corrugated surfaces considered, since it defines the virtual origin of the mean flow, and thus both the *virtual* inner radius,

$$R_{i\,\mathrm{vrt}} = R_i - \hat{\ell}_x \tag{27}$$

and the *virtual* gap thickness,

$$d_{\mathrm{vrt}} = d\,(1 + \epsilon\,\ell_x) \tag{28}$$

on account of Eq. (32), see below, as sketched in Fig. 7. The existence of a virtual radial gap in the case of grooved walls was proposed also by Xu et al.[12] (they called this the *actual gap*). They arbitrarily set the actual/virtual gap thickness equal to half the riblet height, for each case tested; the approximation committed was later used to define the total error bar (comprehensive of measurement errors) in their experimental results on the drag reduction/increase caused by the presence of azimuthal riblets at the inner cylindrical wall of a TC apparatus.

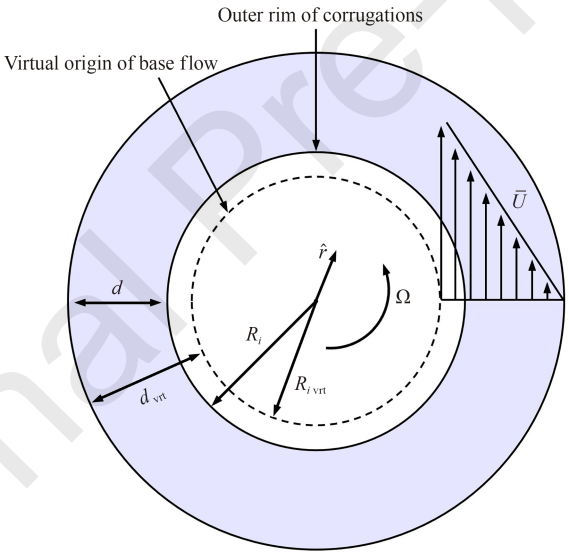


Fig. 7 Sectional sketch of rotating system (dashed circumference highlights inner-wall virtual origin, where dimensionless mean azimuthal velocity is $\bar{U} = 1$).

Numerical solutions of the two auxiliary systems, that for $u^\dagger$ and that for $(v^\dagger, w^\dagger, p^\dagger)$, are obtained using the freefem++ solver,[23] with piecewise $P_2$ continuous finite elements (except for $p^\dagger$ which is discretized with continuous piecewise-linear elements) on an unstructured grid composed by up to 200000 triangular elements in the domain, with refinement near the solid boundary, to guarantee grid-converged solutions. For uniqueness a condition must also be imposed on $p^\dagger$: in our case, the integral of $p^\dagger$ on the domain is forced to vanish. For the idealized micro-corrugations shown in Fig. 2, the dimensionless values found for the slip coefficient are given in Table 2. On account of arguments presented by Luchini et al.,[8] it is

not the individual value of $\ell_x$ (origin of the mean flow) or $\ell_z$ (origin of the cross-stream flow) which affects drag reduction (or, in the present case the onset of the instability), but their difference, since the origin of the wall-normal axis is set arbitrarily. This will be conclusively demonstrated in Section 4.2.

For idealized $S$-type grooves we find $\Delta\ell = \ell_x - \ell_z = 0.023$, while $T$-riblets have $\Delta\ell = 0.094$; we thus expect trapezoidal micro-structures at the wall to have a stronger effect on the onset of Taylor vortices. Sample results of the auxiliary fields for $T$ grooves are provided in Fig. 8.

Table 2 Dimensionless slip lengths for idealized $S$ and $T$ grooves of Fig. 2.

| Micro-groove type | $\ell_x$ | $\ell_z$ |
|---|---|---|
| $S$ | 0.041 | 0.018 |
| $T$ | 0.175 | 0.081 |

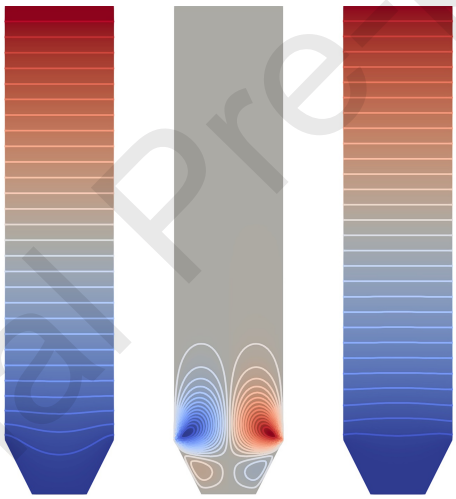

Fig. 8 Auxiliary fields for idealized trapezoidal micro-corrugations ($u^\dagger$ with values in dimensionless range [0, +4.175] (left), $v^\dagger$ [-0.037, +0.037] (middle) and $w^\dagger$ [0, +4.081] (right)).

Since, as shown earlier (Fig. 3), the actual shapes manufactured can be quite different from the ideal ones, in Fig. 9 the result of a sample simulation is shown for the $S1000$ case. The effective corrugation has been modelled with piecewise linear or parabolic segments (cf. bottom three frames in the figure). In this case, the slip coefficients turn out to be slightly larger than the idealized values of Table 2, their dimensionless values being $\ell_x = u^\dagger\big|_{y_\infty} - y_\infty = 0.051$ and $\ell_z = w^\dagger\big|_{y_\infty} - y_\infty = 0.027$.

For all azimuthally-invariant *realistic* corrugations modelled and computed, it is found that $y_\infty = 2.5$ is sufficient to yield results of the $\cdot^\dagger$ variables which become independent of $z$ at the upper boundary of the unit cell, for $\ell_x$ and $\ell_z$ to attain values independent of

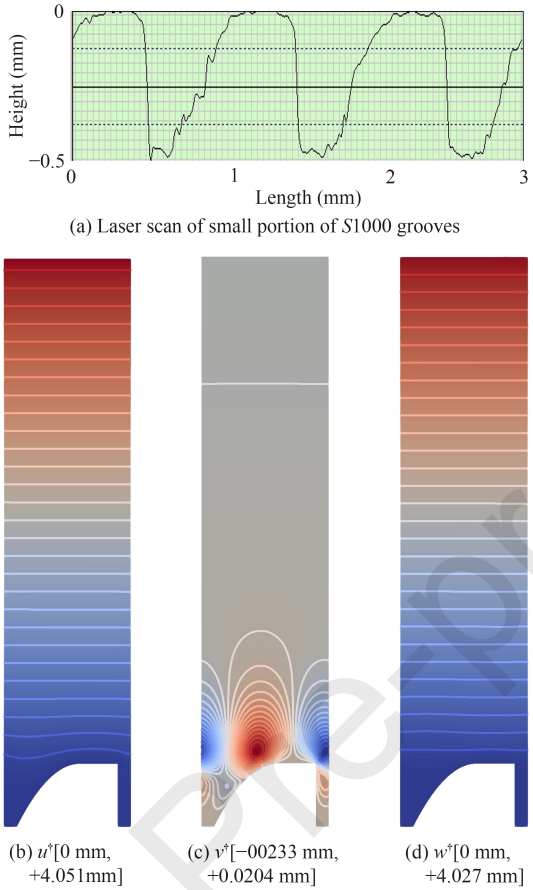


(a) Laser scan of small portion of $S1000$ grooves

(b) $u^{\dagger}$[0 mm, +4.051mm] (c) $v^{\dagger}$[−00233 mm, +0.0204 mm] (d) $w^{\dagger}$[0 mm, +4.027 mm]

Fig. 9 Laser scan of small portion of $S1000$ grooves and results of $u^{\dagger}$ [0 mm, +4.051 mm], $v^{\dagger}$ [−0.0233 mm, +0.0204 mm] and $w^{\dagger}$ [0 mm, +4.027 mm] for simulated model of *real* corrugations.

$y_{\infty}$. At the outer $y$-edge of the computational domain it is also found that $v^{\dagger}\big|_{y_{\infty}} = 0$. The vertical size of the *real* corrugations is measured to be 476 µm instead of the imposed value $\ell/2 = 500$ µm. All the computed slip lengths are provided in Table 3. It should be observed that, contrary to the $S$-case, the 3D-printed trapezoidal grooves have smaller slip lengths than their idealized counterparts. The fact that $T$-riblets yield larger slip coefficients than $S$-riblets of same spanwise pitch is consistent with the literature.[8,9,24]

Table 3 Dimensional slip lengths and differential slip ($\Delta\hat{\ell} = \hat{\ell}_x - \hat{\ell}_z$) from homogenization calculations for reconstructed, *realistic* geometries, together with *virtual* dimensions of different microstructured surfaces.

| Case | $\hat{\ell}_x$ | $\hat{\ell}_z$ | $\Delta\hat{\ell}$ | $R_{i\,\mathrm{vrt}}$ | $d_{\mathrm{vrt}}$ | $R_m$ | $\eta_{\mathrm{vrt}}$ |
|---|---|---|---|---|---|---|---|
| $T400$ | 0.046 (0.070) | 0.026 (0.032) | 0.020 (0.038) | 18.65 | 1.99 | 19.64 | 0.904 |
| $T800$ | 0.107 (0.140) | 0.055 (0.065) | 0.052 (0.075) | 18.74 | 1.90 | 19.69 | 0.908 |
| $T1000$ | 0.134 (0.175) | 0.069 (0.081) | 0.065 (0.094) | 18.82 | 1.82 | 19.73 | 0.912 |
| $S800$ | 0.041 (0.033) | 0.021 (0.014) | 0.020 (0.019) | 18.78 | 1.86 | 19.71 | 0.910 |
| $S1000$ | 0.051 (0.041) | 0.027 (0.018) | 0.024 (0.023) | 18.91 | 1.73 | 19.77 | 0.916 |

Notes: *Idealized* slip values are given within round brackets for each shape and periodicity examined. *Virtual* mean radius, $R_m = (R_{i\,\mathrm{vrt}} + R_o)/2$, and radius ratio, $\eta_{\mathrm{vrt}} = R_{i\,\mathrm{vrt}}/R_o$, are also defined. All units are mm aside for $\eta_{\mathrm{vrt}}$ which is dimensionless.

## 4. The stability theory

The steady flow upon which small perturbations are superposed is easily retrieved from Equation (10), subject to boundary condition (24) at $Y = 0$ and no-slip at $Y = 1$, upon further assuming that $V = W = 0$. The mean azimuthal flow, now indicated with an overbar, $\bar{U}$, is invariant with respect to slow axial variable $Z$ and reads

$$\bar{U}(Y) = A_1\, e^{-\delta Y} + A_2 \tag{29}$$

with

$$\begin{cases} A_1 = \dfrac{1}{1 + \epsilon\,\delta\,\ell_x - e^{-\delta}} \\ A_2 = \dfrac{-e^{-\delta}}{1 + \epsilon\,\delta\,\ell_x - e^{-\delta}} \end{cases} \tag{30}$$

The slip velocity at the virtual wall is

$$\bar{U}(0) = 1 - \epsilon\,\ell_x + \mathcal{O}(\epsilon\,\delta) + \mathcal{O}(\epsilon^2) \tag{31}$$

while the (negative) $Y$-position where $\bar{U} = 1$ is

$$Y = -\frac{1}{\delta}\ln\left[1 + \epsilon\,\delta\,\ell_x\right] = -\epsilon\,\ell_x + \mathcal{O}(\epsilon^2\,\delta) \tag{32}$$

The linear stability problem is treated by assuming that the base flow velocity and pressure fields are perturbed by infinitesimal disturbances (denoted by primes) as

$$U = \bar{U} + U' \tag{33}$$
$$V = V' \tag{34}$$
$$W = W' \tag{35}$$
$$P = \bar{P} + P' \tag{36}$$

The linearized disturbance equations are:

$$\frac{\partial V'}{\partial Y} + \delta V' + \frac{\partial W'}{\partial Z} = 0 \tag{37}$$

$$\frac{\partial V'}{\partial T} - 2\delta \bar{U} U' = -\frac{\partial P'}{\partial Y} + \frac{1}{Re}\left(\frac{\partial^2 V'}{\partial Y^2} + \delta \frac{\partial V'}{\partial Y} + \frac{\partial^2 V'}{\partial Z^2}\right) \tag{38}$$

$$\frac{\partial U'}{\partial T} + V' \frac{\partial \bar{U}}{\partial Y} + \delta \bar{U} V' = \frac{1}{Re}\left(\frac{\partial^2 U'}{\partial Y^2} + \delta \frac{\partial U'}{\partial Y} + \frac{\partial^2 U'}{\partial Z^2}\right) \tag{39}$$

$$\frac{\partial W'}{\partial T} = -\frac{\partial P'}{\partial Z} + \frac{1}{Re}\left(\frac{\partial^2 W'}{\partial Y^2} + \delta \frac{\partial W'}{\partial Y} + \frac{\partial^2 W'}{\partial Z^2}\right) \tag{40}$$

The perturbations are written as

$$U' = \tilde{U}(Y)\, e^{\sigma T} \cos(\beta Z) \tag{41}$$

$$V' = \tilde{V}(Y)\, e^{\sigma T} \cos(\beta Z) \tag{42}$$

$$W' = \tilde{W}(Y)\, e^{\sigma T} \sin(\beta Z) \tag{43}$$

$$P' = \tilde{P}(Y)\, e^{\sigma T} \cos(\beta Z) \tag{44}$$

with $\sigma$ a complex number (the real part is the growth rate of the disturbance and the imaginary part is its frequency) and $\beta$ the real, spanwise wavenumber. To simplify notations, $D$ is used to express $\mathrm{d}/\mathrm{d}\,Y$ so that the equations for the mode shapes take the form

$$D\tilde{V} + \delta \tilde{V} + \beta \tilde{W} = 0 \tag{45}$$

$$2\delta \bar{U}\tilde{U} - D\tilde{P} + \frac{1}{Re}[D^2\tilde{V} + \delta D\tilde{V} - \beta^2 \tilde{V}] = \sigma \tilde{V} \tag{46}$$

$$-\tilde{V} D\bar{U} - \delta \bar{U}\tilde{V} + \frac{1}{Re}[D^2\tilde{U} + \delta D\tilde{U} - \beta^2 \tilde{U}] = \sigma \tilde{U} \tag{47}$$

$$\beta \tilde{P} + \frac{1}{Re}[D^2\tilde{W} + \delta D\tilde{W} - \beta^2 \tilde{W}] = \sigma \tilde{W} \tag{48}$$

The boundary conditions are

$$\tilde{U}\big|_{Y=0} = \epsilon \ell_x D\tilde{U}\big|_{Y=0} \tag{49}$$

$$\tilde{V}\big|_{Y=0} = 0 \tag{50}$$

$$\tilde{W}\big|_{Y=0} = \epsilon \ell_z D\tilde{W}\big|_{Y=0} \tag{51}$$

plus vanishing velocity mode shapes at $Y = 1$.

Eqs. (45)-(51) are discretized using second-order finite differences, where the continuity equation and the disturbance pressure are staggered to avoid numerical oscillations. The least stable eigenvalues are computed using an inverse iteration algorithm, while the spectrum of eigenvalues is solved using the QZ algorithm.

*4.1. Stability results and comparison with experiments*

Before presenting the results of the stability calculations, some considerations are in order, based on the classical, no-slip case. Results for smooth cylinders[2,15] demonstrate the increase of the critical Taylor number, $Ta_c$, for the onset of the instability with the reduction of the radius ratio, $\eta$. Conversely, the critical wavenumber, $\beta_c$, increases very slowly when $\eta$ is lowered. As shown in Table 1 the radius ratio $\eta$ of the micro-structured cases increases with the pattern's periodicity, which seems to suggest that a reduction of the critical Taylor number (and a slow decrease of the wavenumber) with respect to the smooth case might be expected.

Calculations with slip conditions at $\hat{r} = R_i$ are conducted for all cases studied, including both the idealized and the modelled corrugations. Dimensions and parameters used to compute results for the idealized model are provided in Table 4; corrugations of height $\ell/2$ and periodicity $\ell$ are assumed to be positioned exactly above the sleeve of the smooth case (thus, for example, the inner radius of the case $T400$, for which $\ell = 0.4$ mm, is taken to be $(18.36 + 0.4/2)$ mm, and similarly for the other cases).

Table 4 Geometrical dimensions and dimensionless parameters used for stability analysis of idealized micro-undulations (in all configurations $R_o$ is fixed and equal to 20.64 mm).

| Case | $R_i$ (mm) | $d$ (mm) | $\ell$ (mm) | $\eta = R_i/R_o$ | $\delta = d/R_i$ | $\epsilon = \ell/d$ |
|---|---|---|---|---|---|---|
| Smooth cylinder | 18.36 | 2.28 | | 0.890 | 0.124 | |
| $T400$ | 18.56 | 2.08 | 0.40 | 0.899 | 0.112 | 0.192 |
| $T800$ | 18.76 | 1.88 | 0.80 | 0.909 | 0.100 | 0.426 |
| $T1000$ | 18.86 | 1.78 | 1.00 | 0.914 | 0.094 | 0.562 |
| $S800$ | 18.76 | 1.88 | 0.80 | 0.909 | 0.100 | 0.426 |
| $S1000$ | 18.86 | 1.78 | 1.00 | 0.914 | 0.094 | 0.562 |

Sample results are provided in Figs. 10 to 12. The first of these three figures displays iso-amplification contours of the most unstable mode for the case $T800$ (idealized micro-undulations) in the $(Re, \beta)$ plane. Mode shapes at the onset conditions for the same case are displayed in Fig. 11, and the non-zero values of $\tilde{U}$ and $\tilde{W}$ at $Y = 0$ are clearly apparent, with the consequent asymmetry of all velocity components around the $Y = 0.5$ midplane. Fig. 11 also highlights a marked asymmetry of the perturbation eigenfunctions with respect to the mid-gap plane at $Y = 0.5$. This asymmetry originates from the mixed boundary conditions imposed at the two walls: a slip condition at the inner cylinder and a no-slip condition at the outer one. As a result, the classical reflection symmetry of the narrow-gap Taylor–Couette problem is broken, leading to eigenmodes whose axial and azimuthal velocity components penetrate differently near the two boundaries. Physically, this implies a slight displacement of the vortex cores toward the inner cylinder. While this asymmetry does not alter the stationary nature of the primary instability, it may influence the detailed roll structure and the subsequent nonlinear saturation. Fig. 12 shows sample spectra, again for $T800$, with the increase of the Reynolds numbers, highlighting the presence of a second unstable mode at $Re \approx 700$, and further unstable modes at larger values of $Re$.

The eigenvalues are either real or form complex conjugate pairs; the fact that it is a real eigenvalue which crosses the imaginary axis at $Re = 150$ in Fig. 12 indicates that the most unstable mode is stationary. Isocontours of the growth rate of the most unstable mode for the different configurations in Table 3 are similar to those reported in Fig. 10.

Results relative to the critical conditions for the onset of the Taylor vortices are summarized in Table 5. The calculations with a slip boundary appear to confirm the qualitative trend based on the virtual origin model regarding the mild increase of the critical Reynolds number with the pattern periodicity, for both square and trapezoidal shapes. The Reynolds numbers of the realistic grooves exceed the idealized ones, for both $T$ and $S$ grooves and for all values of $\ell$. Conversely, the critical Taylor number does not exhibit a monotonic trend with the pitch $\ell$ of the micro-roughness elements. A discussion on this is deferred to the next subsection.

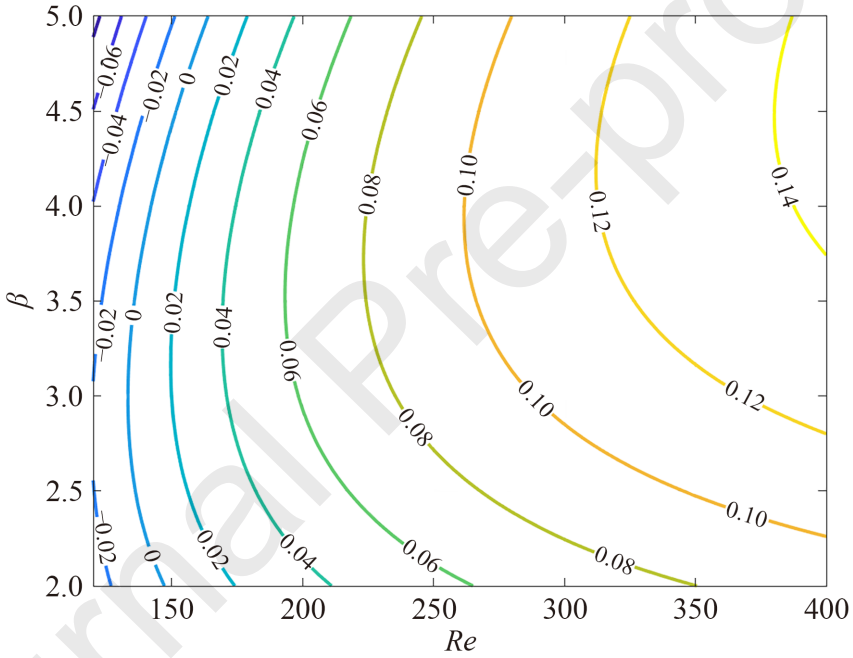


Fig. 10 Contours of growth rate ($\sigma_r$) of case $T800$ for idealized micro-groove shape (Critical conditions are $Re_c = 133.4$ ($Ta_c = 1698$), $\beta_c = 2.983$).

It is also interesting to notice the rather large deviation in the values of the critical wavenumber, $\beta_c$, between the theoretical and the laboratory results for the different textured surfaces. We believe that this is due to the weak wavelength selection mechanism, clearly evidenced by the iso-amplification curves in Fig. 10. Because of this, the naturally appearing wavelength is strongly affected by the type, periodicity and amplitude of the surface texture, resulting in $\beta_c$-variations which can reach 18% (for the case $T1000$) with respect to the reference value.

The effect of the curvature parameter $\eta$ on the critical conditions is described by Fig. 13, where $Ta_c$ and $Re_c$ are plotted together with the reference no-slip stability results, computed by the same code used so far while enforcing $\tilde{U}\big|_{Y=0} = \tilde{V}\big|_{Y=0} = \tilde{W}\big|_{Y=0} = 0$ at the inner wall.

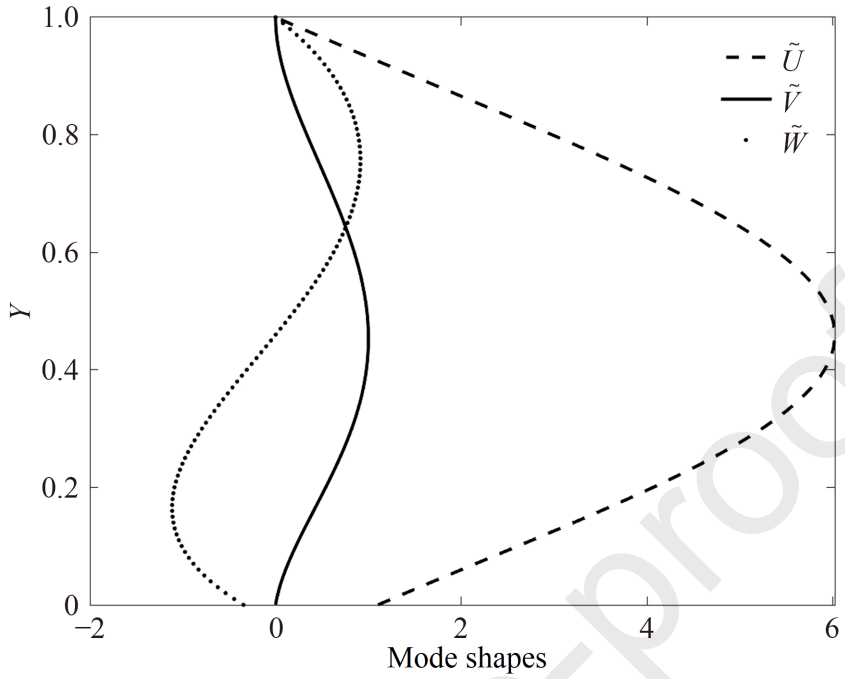


Fig. 11 Perturbation velocity components, scaled with $\max(\tilde{V})$, as a function of radial direction, for case $T800$ at onset conditions: $Re_c = 133.4$, $\beta_c = 2.983$.

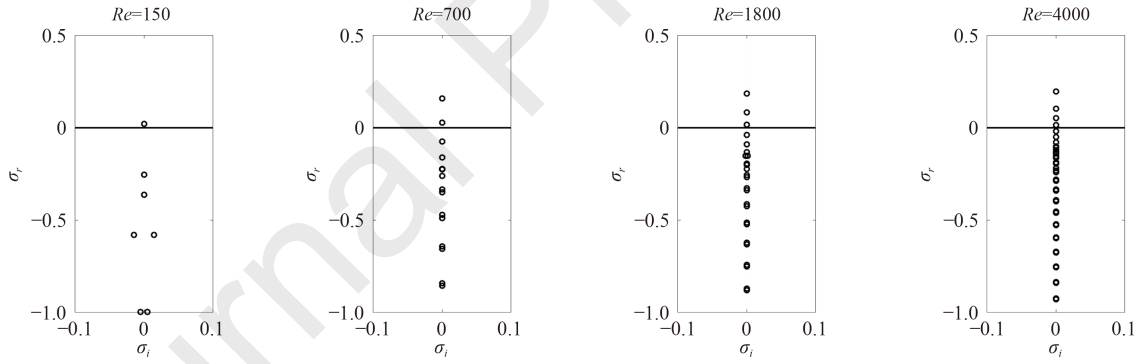


Fig. 12 Eigenvalue spectrum of case $T800$ with idealized shape for $\beta = \pi$.

The results displayed, beyond demonstrating visually an acceptable qualitative agreement between experiments and theory, appear to indicate that the instability occurs earlier than in the reference no-slip case, for each value of $\eta$ (aside for one case). This aspect will be further examined in the next section.

The numerical and experimental results in Table 5 for both $T$ and $S$ grooves also indicate that the wavenumber at onset decreases slowly with $\ell$. At this point, it should be noticed that all of the results in Table 5 are scaled with $R_i$ and $d = R_o - R_i$; since the fluid can penetrate below the outer rim of the corrugation, the available (radial) space for the vortex

Table 5 Onset conditions for both theoretical and experimental results.

| Case | Theory: idealized shapes ($\eta$, $Re_c$, $Ta_c$, $\beta_c$) | Theory: realistic shapes ($\eta$, $Re_c$, $Ta_c$, $\beta_c$) | Laboratory results ($\eta$, $Re_c$, $Ta_c$, $\beta_c$) |
|---|---|---|---|
| Smooth cylinder | (0.890, 121.8, 1735, 3.143) | (0.890, 121.8, 1735, 3.143) | (0.890, 122.2, 1746, 3.1) |
| $T400$ | (0.899, 127.1, 1714, 3.050) | (0.906, 131.1, 1696, 3.070) | (0.906, 134.1, 1772, 2.8) |
| $T800$ | (0.909, 133.4, 1698, 2.983) | (0.913, 136.0, 1675, 3.010) | (0.913, 134.6, 1618, 3.1) |
| $T1000$ | (0.914, 137.3, 1699, 2.950) | (0.918, 139.9, 1670, 2.983) | (0.918, 140.2, 1679, 3.5) |
| $S800$ | (0.909, 134.5, 1726, 3.090) | (0.912, 135.7, 1700, 3.077) | (0.912, 137.0, 1732, 2.9) |
| $S1000$ | (0.914, 138.2, 1721, 3.084) | (0.919, 140.8, 1683, 3.070) | (0.919, 143.3, 1731, 3.2) |

Notes: The former are computed for both idealized and modelled micro-grooves, using values of $\delta$ and $\epsilon$ from Table 4 (*idealized* case) and Table 1 (*realistic* case), together with slip coefficients in Table 3.

is really $d_{\mathrm{vrt}}$ and not $d$ (Fig. 7). The wavenumbers, scaled with $d_{\mathrm{vrt}}$, are close to $\pi$ for all numerical cases considered (see later Table 6), meaning that at the onset the rolls maintain a square aspect ratio.

### *4.2. Is instability postponed or anticipated?*

Just as the appropriate scale for the vortex wavelength needs the use of the virtual gap of the system, we now rescale the Reynolds and Taylor numbers using the virtual inner radius ($R_{i\,\mathrm{vrt}} = R_i - \hat{\ell}_x$) and the virtual gap ($d_{\mathrm{vrt}} = d + \hat{\ell}_x$); we do the same also for the radius ratio, $\eta$, and the torque coefficient, $c_T$, denoting, in each case, the new parameter by the subscript vrt.

The experimental results of Fig. 5, rescaled as indicated above, are plotted in Fig. 14. In the subcritical range of Taylor numbers, the quasi-perfect collapse of the curves for the trapezoidal grooves strongly suggests that the scaling based on the virtual dimensions is appropriate. On the other hand, measurements for square grooves do not display a perfect collapse in the low-$Ta$ range, a fact that we ascribe to the less-than-perfect manufacturing of the microstructures in this latter case. Defects such as that shown in Figure 4 result in a local alteration of the regular pattern with a consequent disruption of the base motion, leading to a modification of the wall shear stress. Fig. 14 permits to retrieve the critical values of $Ta_{\mathrm{vrt}}$ (and $Re_{\mathrm{vrt}}$) for each case. The results are summarized in Table 6, for both experimental and theoretical cases: the agreement is good particularly for $T$-shaped corrugations, with the rescaled, critical Reynolds and Taylor numbers which consistently increase with the length scale $\ell$ of the wall inhomogeneities.

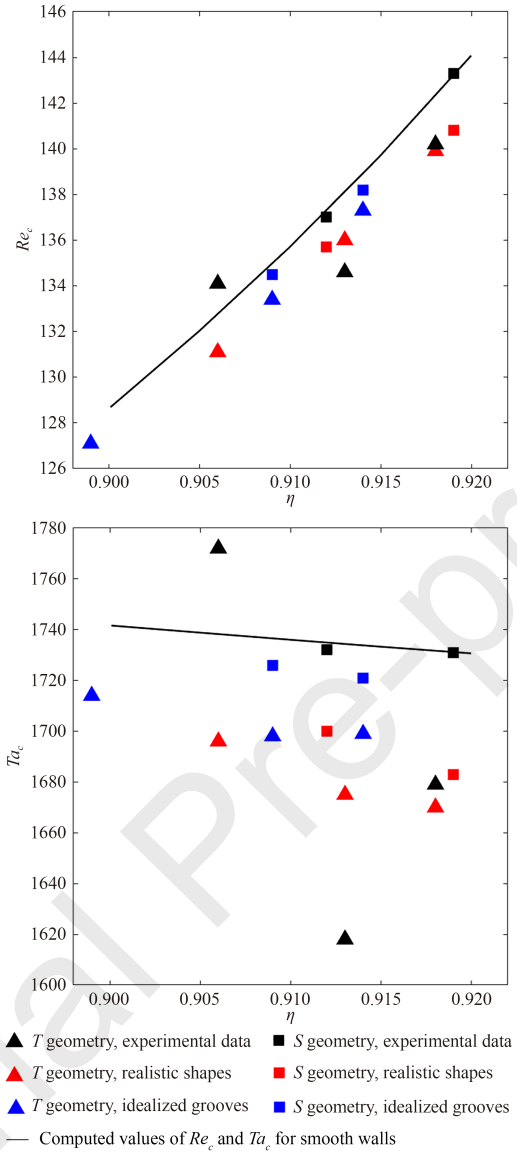


Fig. 13 Critical parameters versus radius ratio (uncertainty on critical Reynolds numbers measured in laboratory (black symbols) is of ±1; this means that error bar on experimental Taylor number is ±25).

The rescaled critical values ($Re_{c\,\mathrm{vrt}}$ and $Ta_{c\,\mathrm{vrt}}$) are, for any value of the radius ratio, above their respective no-slip counterparts, whose values are provided in the two images of Fig. 13, cf. the solid lines. This indicates that (A) azimuthally-invariant grooves are effective at postponing the onset of the instability, and (B) trapezoidal corrugations are more effective than square-shaped ones. This latter observation is consistent with the fact that the increase in the critical value of $Ta$ (or $Re$) depends at leading order on the difference between the two protrusion heights, $\Delta\ell = \ell_x - \ell_z$. This is the case, just like for riblets in a turbulent channel or boundary layer flow, because any physically significant quantity cannot

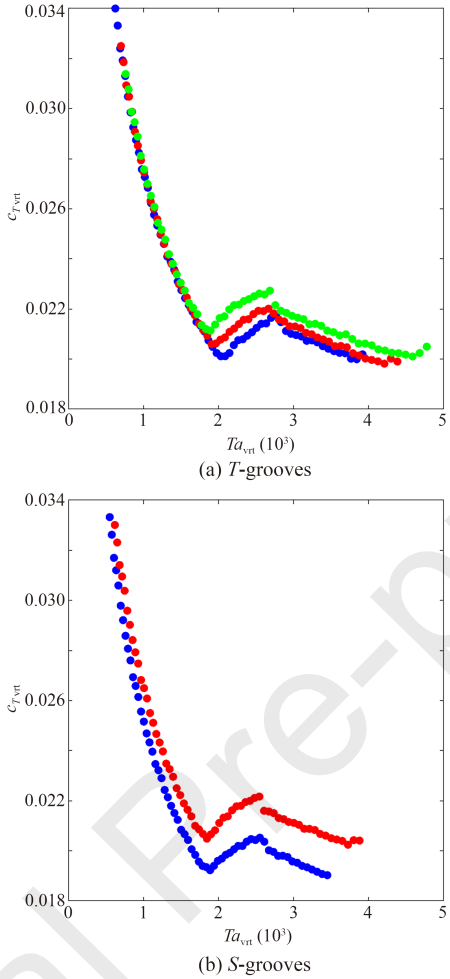


Fig. 14 Same as Fig. 5, after rescaling axes using virtual origin of mean azimuthal flow.

Table 6 Onset conditions based on rescaled (virtual) dimensions of gap and inner radius.

| Case | Theory: idealized shapes $(\eta_c,\ Re_c,\ Ta_c,\ \beta_c)_{\mathrm{vrt}}$ | Theory: realistic shapes $(\eta_c,\ Re_c,\ Ta_c,\ \beta_c)_{\mathrm{vrt}}$ | Laboratory results $(\eta_c,\ Re_c,\ Ta_c,\ \beta_c)_{\mathrm{vrt}}$ |
|---|---|---|---|
| $T400$ | (0.896, 130.9, 1882, 3.153) | (0.904, 133.9, 1812, 3.143) | (0.904, 136.9, 1894, 3.0) |
| $T800$ | (0.902, 142.3, 2083, 3.205) | (0.908, 143,3, 1979, 3.190) | (0.908, 141.0, 1915, 3.5) |
| $T1000$ | (0.905, 149.4, 2219, 3.240) | (0.912, 149.9, 2078, 3.220) | (0.912, 150.3, 2088, 4.1) |
| $S800$ | (0.907, 136.6, 1814, 3.144) | (0.910, 138.5, 1810, 3.146) | (0.910, 139.8, 1846, 3.1) |
| $S1000$ | (0.912, 141.1, 1837, 3.155) | (0.916, 144.7, 1832, 3.163) | (0.916, 146.7, 1887, 3.4) |

depend on the choice of the origin (here set at the tip of the grooves); the only combination of the two protrusion heights that plays a role is their difference, i.e. the separation between the two virtual walls seen by azimuthal and axial flow. For the case of the critical $Re$ we

can thus write, for each value of the radius ratio, that

$$Re_{c\,\mathrm{vrt}} = Re_{c\,\mathrm{smooth}} + \zeta \left.\frac{\partial Re_c}{\partial \zeta}\right|_{\zeta=0} + \mathcal{O}(\zeta^2) \tag{52}$$

and likewise for the Taylor number, with $Re_{c\,\mathrm{smooth}}$ the critical value of the Reynolds number for the case of a smooth wall, and the dimensionless parameter $\zeta$ given by

$$\zeta = \frac{\Delta\hat{\ell}}{d_{\mathrm{vrt}}} = \epsilon_{\mathrm{vrt}}\Delta\ell \tag{53}$$

with $\epsilon_{\mathrm{vrt}} = \ell/d_{\mathrm{vrt}} \ll 1$.

The stabilizing influence of differential slip arises from a combination of effects rather than from a single mechanism. Anisotropic slip modifies the effective geometry of the system, the centrifugal balance, and the boundary conditions experienced by the perturbations. Among these, the dominant contribution at leading order is the effective widening of the gap perceived by the instability. In classical Taylor–Couette flow with inner-cylinder rotation, a wider gap leads to higher critical Reynolds and Taylor numbers due to reduced centrifugal destabilization per unit radial distance and weaker confinement of Taylor vortices. In the present configuration, the separation between the virtual origins of azimuthal and axial motion produces an analogous effect. Local modifications of the base-flow shear and anisotropic perturbation boundary conditions provide secondary contributions, which may influence modal structure and nonlinear saturation but do not control the onset threshold.

Fig. 15 shows both $\Delta Re_c = Re_{c\,\mathrm{vrt}} - Re_{c\,\mathrm{smooth}}$ and $\Delta Ta_c = Ta_{c\,\mathrm{vrt}} - Ta_{c\,\mathrm{smooth}}$ versus $\zeta$ for all cases treated numerically and confirms that, provided that $\zeta$ is small enough, the variations in Reynolds and Taylor numbers follow a linear trend; the scatter in the data is very low, as expected, since the variation in radius ratio among the different cases is not large. These results permit to state that we achieve the largest increase in critical Reynolds (or Taylor) number, or, in other words, the instability can be postponed the most, with circumferential microgrooves which maximize $\Delta\ell$. This occurs for very thin blade riblets.[8,9]

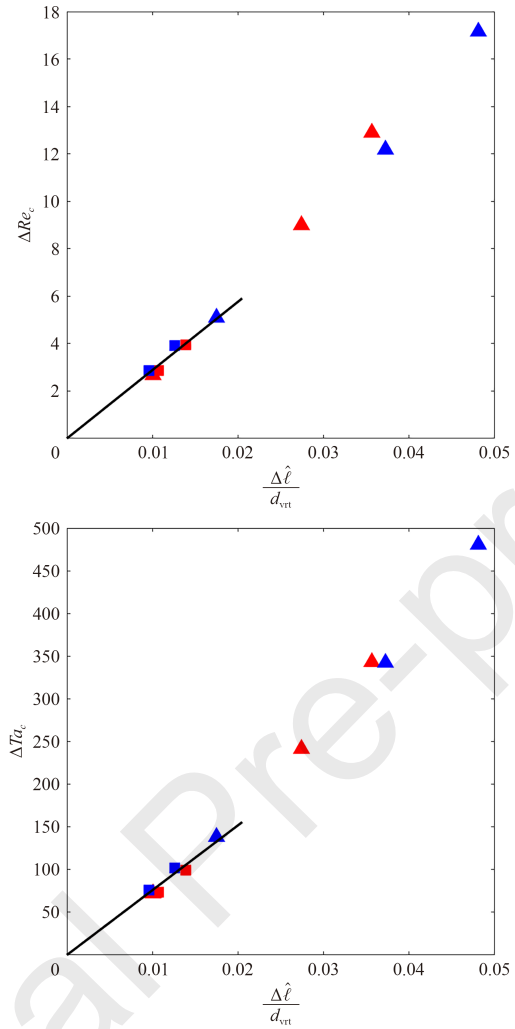


Fig. 15 Variations of critical Reynolds and Taylor numbers (with respect to corresponding smooth-wall cases) versus $\Delta\hat{\ell}/d_{\mathrm{vrt}}$ for all configurations simulated (Symbols are as in Fig. 13. Straight, solid lines are plotted only to guide eyes).

## 5. Conclusions

A comprehensive investigation has been conducted to understand the influence of circumferential microgrooves on the onset of the primary Taylor–Couette instability. Microstructured sleeves with trapezoidal and square grooves were manufactured via stereolithographic printing, and their effect was characterized both experimentally, by torque measurements and flow visualizations, and theoretically, through an asymptotic homogenization approach, which stops at leading order in $\epsilon$ (yielding effective slip boundary conditions), plus a linear stability analysis. Higher-order homogenization terms are not expected to significantly change the macroscopic results, as shown, e.g., by Bottaro and Naqvi.[18]

The results demonstrate that azimuthally invariant microgrooves alter the stability char-

acteristics of the system in a subtle but systematic way. When the critical parameters are expressed in terms of the geometrical dimensions of the physical setup, the grooves appear to promote instability, leading to an earlier onset of Taylor vortices compared to smooth walls (Fig. 13). However, once the concept of virtual origin of the mean azimuthal flow is introduced and the parameters are rescaled accordingly, it becomes clear that the instability is in fact postponed. The degree of delay increases with the groove pitch and is more pronounced for trapezoidal microstructures than for square ones, consistent with the larger difference in slip lengths ($\Delta\ell$) obtained for the former.

These findings underline two main points: first, mildly corrugated walls can be effectively modeled by Navier slip conditions within a homogenization framework, thereby offering a powerful and computationally efficient tool to account for surface roughness in stability analyses. Second, the design of microgroove geometry provides a viable strategy to control the onset of centrifugal instabilities, with direct implications for delaying transition in rotating shear flows, with potential applications ranging from rotating machinery and journal bearings, where early vortex formation increases losses and vibrations, to cylindrical mixers and reactors, where the control of centrifugal instabilities can be used to tune momentum and heat transport.

Future work should extend the present analysis beyond the primary instability, considering regimes where advection and nonlinear interactions become relevant. In particular, the present homogenization–stability framework could be applied to the onset of wavy vortex flow and to non-axisymmetric instabilities, where wall-induced anisotropy may play a more prominent role. Another natural extension concerns higher rotation rates and weakly turbulent regimes, where effective slip models may still provide valuable insight into the modification of near-wall structures. Furthermore, the approach could be generalized to azimuthally non-invariant textures, such as helical or staggered grooves, as well as to superhydrophobic or lubricant-infused surfaces, allowing a systematic comparison of different surface designs within a unified virtual-origin framework.

**Acknowledgements**

The research of the group from Genova was partially funded by the European Union - NextGenerationEU (Piano Nazionale di Ripresa e Resilienza, Missione 4 Componente 2 Investimento 1.4 "Potenziamento strutture di ricerca e creazione di "campioni nazionali di R&S" su alcune Key Enabling Technologies"). (CN00000023)— Title: "Sustainable Mobility Center (Centro Nazionale per la Mobilità Sostenibile - CNMS)", CUP D33C22000940007. ES and NM would like to thank the French National Research Agency (ANR) for its financial support under the IDEFHYX project (ANR-22-CE51-0021). We are grateful to Prof. Enrico Lertora and Prof. Marco Pizzorni for their support with the laser measurements of the corrugations; Prof. Corrado Boragno and Prof. Edward Canepa are acknowledged for their constructive feedback on the visualization of the Taylor vortices. We thank Mr. Luca Labesse for conducting some experiments in the late stages of this research, to verify previously obtained results.

## Appendix A. Experimental end effects

To account for end effects, particularly for the fluid motion caused by the rotation of the conical endtip of the rotating setup, we have run cases with the free water surface exactly in correspondence of the junction between the cylinder and the bottom cone. Tests have been run for angular velocities increasing from 20 to 50 r/min, with the same experimental protocol used previously. Measurements of the torque, $\mathcal{C}$, are displayed in Fig. A1 for the case of smooth cylinders; the upper experimental points (red symbols) corresponds to the untreated set of data, taken at an average temperature of 25.7 °C. The middle set of points (blue symbols) represent the same dataset from which, however, the results for the measurements with only the cone completely immersed (same temperature as before, green symbols), have been subtracted. The rationale for this is that, at low rotational speed, the influence of the fluid motion in the lower part of the setup can be simply subtracted to eliminate end effects. The success of the assumption above can be evaluated by comparing the slope of the straight line tangent to the data points in the interval $\dot{n} \in [20, 24]$ with the exact solution for the torque when the flow is one-dimensional, i.e. before the onset of the instability. The dashed straight line stems from the expression $\mathcal{C} = -\mu \dfrac{\mathrm{d}\hat{u}_\theta}{\mathrm{d}\hat{r}}\bigg|_{\hat{r}=R_i} 2\pi R_i^2 H$, with $\hat{u}_\theta(\hat{r}) = \Omega R_i \bar{U}(Y)$ the Couette velocity distribution in the gap and $Y = (\hat{r} - R_i)/d$ (cf. Sections 3 and 4 for notations). The theoretical curve is slightly off the experimental line and it sits below it; this is ascribed to two effects in the experiments:

(1) The vortices near the free surface at the top differ from those which are formed in an infinitely long setup;

(2) Vortical disturbances induced by the rotating cone appear even at low rotational speed; they can then diffuse upwards and increase the shear stress at the cylinder wall, even in subcritical conditions.

The mild disagreement between theory and experiments is of the order of 0.2 nanoNewton meter when $\dot{n}$ is 20 r/min and bears no consequences on the definition of the instability onset, which can rather precisely be set at $\dot{n} = 24.5 \pm 0.3$ r/min. At the mean temperature and viscosity at which the measurements have been carried out, this corresponds to a critical Reynolds number equal to $Re_c = 122.2 \pm 1.5$.

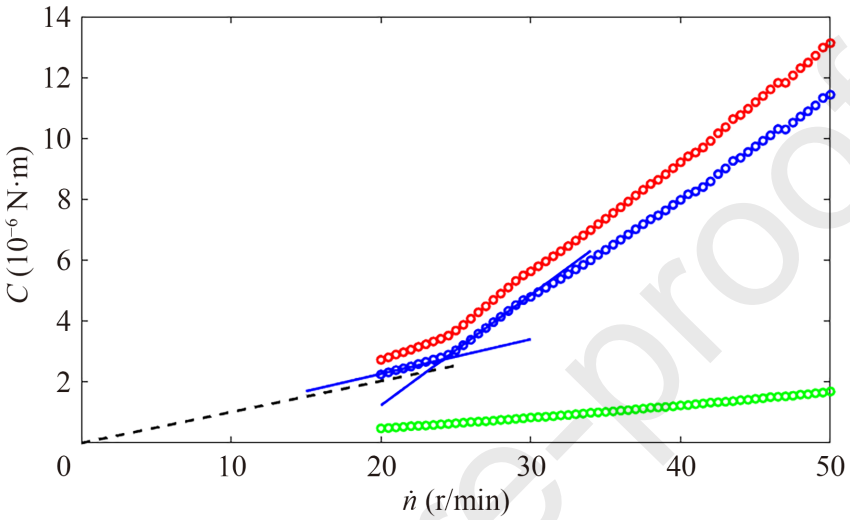


Fig. A1 Torque versus rotation speed for smooth case. Intersection between two straight, blue lines, tangent to data points, defines first bifurcation to Taylor vortices. Black dashed line represents analytical result for case of infinite cylinders (for explanation of meaning of colors, see text.)

## References


1. Taylor GI. Stability of a viscous liquid contained between two rotating cylinders. *Philos Trans R Soc Lond Ser A* 1923;**223**(605-615):289–343.

2. Chandrasekhar S, *Hydrodynamic and hydromagnetic Stability*. New York: Dover Publications, Inc.; 1981.p.310.

3. Srinivasan S, Kleingartner JA, Gilbert JB, et al. Sustainable drag reduction in turbulent Taylor-Couette flows by depositing sprayable superhydrophobic surfaces. *Phys Rev Lett* 2015;**114**:014501.

4. Naim MS, Baig MF. Turbulent drag reduction in Taylor-Couette flows using different super-hydrophobic surface configurations. *Phys Fluids* 2019;**31**:095108.

5. Liu X, You CX, Cao YL, et al. Friction drag reduction of Taylor–Couette flow over air-filled microgrooves. *J Fluid Mech* 2024;**999**:A63.

6. Van Buren T, Smits AJ. Substantial drag reduction in turbulent flow using liquid-infused surfaces. *J Fluid Mech* 2017;**827**:448–56.

7. Bechert DW, Bartenwerfer M. The viscous flow on surfaces with longitudinal ribs. *J Fluid Mech* 1989;**206**:105–29.

8. Luchini P, Manzo F, Pozzi A. Resistance of a grooved surface to parallel flow and cross-flow. *J Fluid Mech* 1991;**228**:87–109.

9. Bechert DW, Bruse M, Hage W, et al. Experiments on drag-reducing surfaces and their optimization with an adjustable geometry. *J Fluid Mech* 1997;**338**:59–87.

10. Hall T, Joseph D. Rotating cylinder drag balance with application to riblets. *Exp Fluids* 2000;**29**(3):215–27.

11. Greidanus AJ, Delfos R, Tokgoz S, et al. Turbulent Taylor–Couette flow over riblets: drag reduction and the effect of bulk fluid rotation. *Exp Fluids* 2015;**56**(5):107.

12. Xu B, Li H, Liu X, et al. Effects of micro-grooves on drag reduction in Taylor-Couette flow. *Phys Fluids* 2023;**35**(4):043608.

13. Zhu X, Ostilla-Mónico R, Verzicco R, et al. Direct numerical simulation of Taylor–Couette flow with grooved walls: torque scaling and flow structure. *J Fluid Mech* 2016;**794**:746–74.

14. Jouin A, Robinet JC, Cherubini S. Modal and nonmodal stability of the laminar flow in a channel with longitudinal riblets. *Phys Rev Fluids* 2024;**9**:073903.

15. Koschmieder EL, *Bénard Cells and Taylor Vortices*. New York, N.Y.: Cambridge University Press; 1993.p.217.

16. Bottaro A. Flow over natural or engineered surfaces: an adjoint homogenization perspective. *J Fluid Mech* 2019;**877**:P1.

17. Zampogna GA, Magnaudet J, Bottaro A. Generalized slip condition over rough surfaces. *J Fluid Mech* 2019;**858**:407–36.

18. Bottaro A, Naqvi SB. Effective boundary conditions at a rough wall: a high-order homogenization approach. *Meccanica* 2020;**55**:1781–800.

19. Lācis U, Sudhakar Y, Pasche S, et al. Transfer of mass and momentum at rough and porous surfaces. *J Fluid Mech* 2020;**884**:A21.

20. Naqvi SB, Bottaro A. Interfacial conditions between a free-fluid region and a porous medium. *Int J Multiph Flow* 2021;**141**:103585.

21. Sudhakar Y, Lācis U, Pasche S, et al. Higher-order homogenized boundary conditions for flows over rough and porous surfaces. *Transp Porous Media* 2021;**136**:1–42.

22. Bottaro A, Innocenti G, Ahmed EN. A slip-transpiration-vortex model for riblets past the viscous regime. *Meccanica* 2025;**60**:2487–506.

23. Hecht F. New development in freefem++. *J Num Math* 2012;**20**(3-4):251–65.

24. García-Mayoral R, Jiménez J. Drag reduction by riblets. *Philos Trans A Math Phys Eng Sci* 2011;**369**:1412-27.

The authors declare that there is no financial/personal interest or belief that could affect their objectivity in the paper submitted to the Chinese Journal of Aeronautics.